# Section 6

Developments in global forecast models, case studies, predictability investigations, global ensembles.

# Impact of the 1D sea-ice model GELATO in the global model ARPEGE.

by Eric Bazile[1], Niramson Azouz [1], Adrien Napoly [1] and Cécile Loo [1]

[1]Météo-France & CNRS. (CNRM-UMR 3589) Toulouse. France. *E-mail: eric.bazile@meteo.fr*

## 1 Introduction.

In the global model ARPEGE, used in operations for numerical weather prediction (NWP) at Météo-France the sea-ice representation is still very simple. There is no specific model activated and the temperature over the sea-ice, which remains constant over the forecast, is based on a climatology. With the recent introduction of the SURFEXv8 (July 2019) platform in the Météo-France system, the use of the GELATO-1d sea ice model (Salas y Mélia, 2002) in the ARPEGE NWP became possible. Several technical modifications were necessary in the surface assimilation to ensure a coherent treatment between observations of sea-surface temperature, sea-ice fraction and new prognostic variables of GELATO.

Within the APPLICATE project and the Year Of Polar Prediction (YOPP) program, the coupling of the sea-ice model has been evaluated first with the "previous" operational configuration of ARPEGE T1198c2.2L105 (high resolution over Europe 7.5km) for the two Special Observing Periods (SOP) and with the denied YOPP-SH experiment done with the 4DVar ARPEGE-SH (high resolution area over Antarctica 7.5km) for the SOP3 (15 Nov. 2018 - 15 Feb. 2019).

The evaluation is achieved in the current operational configuration of ARPEGE T1798c2.2L105.

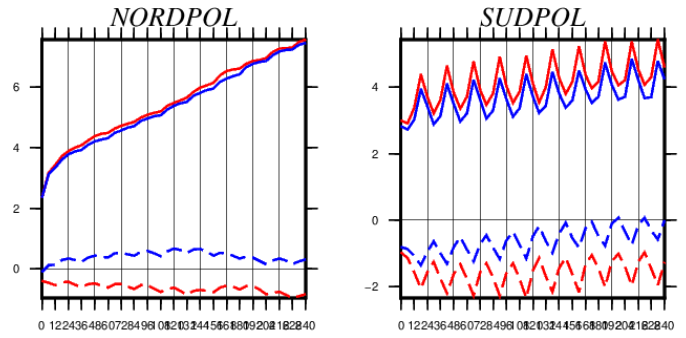


Figure 1: *YOPP-SH SOP3 ARPEGE-SH with GELATO (blue) versus ARPEGE-SH (red). Full line: RMS, dashed line: bias. 60 Forecasts: 10 days lead time*

## 2 The GELATO-1d model

GELATO-1d is a sea-ice model implemented in the SURFEX platform. It is the 1d version of GELATO 6, the sea-ice component of the CNRM-CM6-1 global coupled climate model (Voldoire et al., 2019). Only one category of ice is considered and no horizontal processes are represented.

The model considers 10 layers of ice of equal thickness characterized by their enthalpy and one possible layer of snow covering the ice. The ice fraction per grid cell is constant throughout the forecast and is updated at each analysis (6h) through a weighting of 10% toward the SAF-OSI product. The SST, which corresponds both to the lower condition of the sea-ice slab and the skin temperature of the ice free fraction of the cell, is also constant and follows the OSTIA product.

The surface temperature of the cell is then calculated by weighting the SST and the sea ice temperature calculated by GELATO using the sea-ice fraction.

## 3 Evaluation during the YOPP period

The coupling between the GELATO-1d sea-ice model and ARPEGE has been evaluated with the operational configuration used in 2018 for the YOPP SOP1 and SOP2 period. In addition, two 4Dvar with the ARPEGE-SH configuration (with and without GELATO) have been performed for the YOPP-SH SOP3. The results for the three SOPs are rather similar with a clear warmer sea-ice surface temperature with a positive impact in the boundary layer over the North and South Pole ($|lat| > 60$). Figure 1 shows clearly the improvement of the T2M for the North and the South Pole, the improvement is more significant in Antarctica with more stations along the coast where the sea-ice fraction is non-zero.

For the Emma station in the Ross Ice Shelf area (Fig. 2), the impact of GELATO on the T2M is also very positive and follows the observed values well, except at the end of January by missing the cold event.

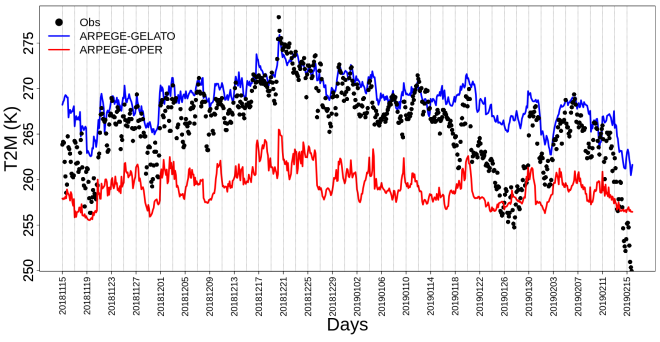


Figure 2: *T2M for the Emma Station (Lat:-84, Lon:-175.01). YOPP-SH SOP3 period (15/11/2018-15/02/2019) with ARPEGE-YOPP-SH*

## 4 Evaluation in the operational configuration

An ARPEGE 4DVar e-suite in T1798L105 (5.5km over Europe) with GELATO has begun the 1st Dec. 2019 with some specific output for the MOSAIC field ex-

periment (https://mosaic-expedition.org/). Figure 3 illustrates the impact of GELATO on the temperature compared to the ECMWF operational analysis considering normalized RMS calculated with 68 forecast from 15 Jan. 2020 to 26 Mar. 2020 Blue lines mean positive impact (%). For the North Pole, the improvement is really significant with a RMS error reduced by 30% below 700hPa. To a lesser extent, the temperatures are also improved over the Antarctic region (Fig. 3) and no clear impact is seen in the tropics (not shown).

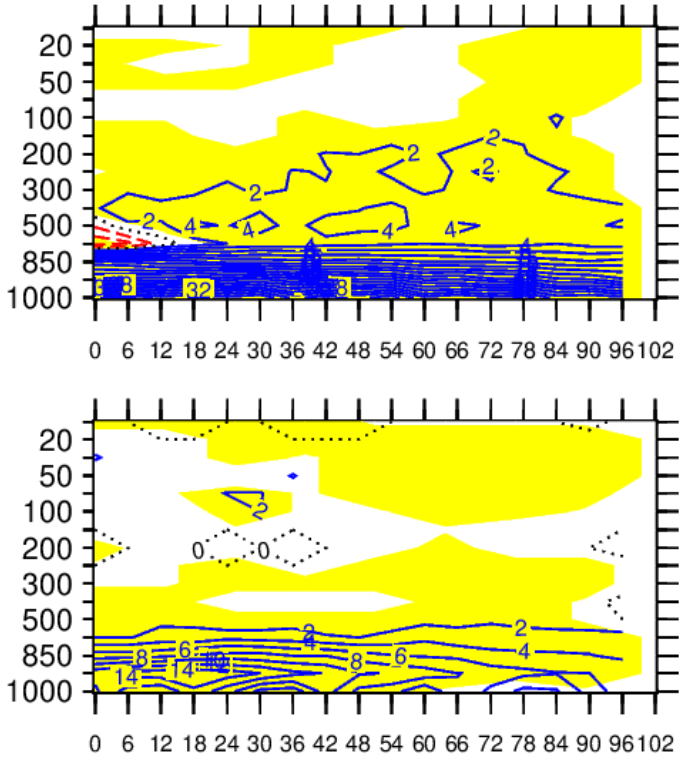


Figure 3: *Impact of the GELATO experiment for the temperature against ECMWF analysis for 20200115-20200326. Blue line: positive impact. X-Axis: lead time (h). Y-Axis: vertical (hPa). Top: North Pole. Bottom: South Pole.*

Thanks to the MOSAiC expedition, a comparison of the T2M is done for the Polarstern track between the 1st Dec. 2019 and 15th Mar. 2020 for the 24h forecast (Fig. 4). This comparison shows clearly the positive impact of the sea-ice model, especially now, the new system is able to follow quite well the warm-cold jump of the T2M seen in observation. However, a warm bias exists (Fig. 2 and 4) notably at the beginning of the period which may be due to an underestimation of the ice/snow thickness or an overestimation of cloud cover. This issue is still under investigation. Figure 5 shows the large impact of the sea-ice model on the T2M for all the area, also seen in Fig. 3 with a warmer boundary layer. During this period (19-21 Feb. 2020), the signature of the warm and moist air advection can be seen only in the ARPEGE-GELATO system.

## 5 Conclusions and perspectives

The coupling of the sea-ice model with the ARPEGE global NWP system has a significant positive impact in the polar regions and over North America. Over Europe (not shown) the improvement is less with a reduction of the temperature RMS by about 4 %. Nowadays, sea-ice thickness observations become available almost in real time and can probably be used in the near future in the sea-ice surface analysis. In addition, thanks to a better sea-ice surface temperature, new satellite channels might be assimilated in Polar Regions. This update will be used in operations beginning of 2021.

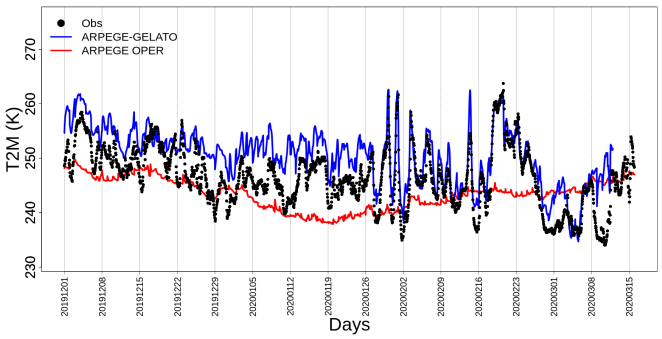


Figure 4: *MOSAIC expedition. T2M from the German icebreaker Polarstern (black). ARPEGE Ref: red. ARPEGE with the sea-ice model: blue.*

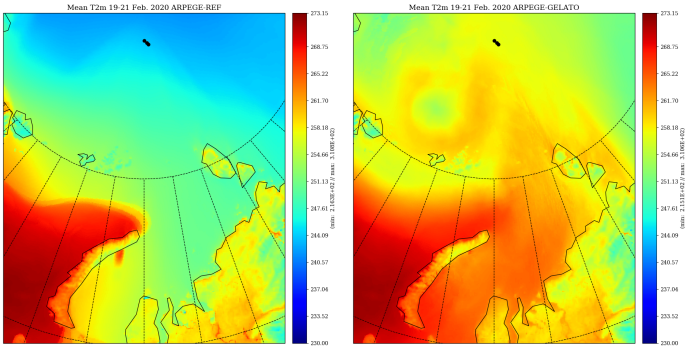


Figure 5: *Mean T2m for 19-20-21 Feb. 2020. Left: ARPEGE Ref. Right: ARPEGE with the sea-ice model. Black dot: Polarstern position for those dates.*

**Acknowledgements:** The authors thank David Salas y Mélia for the fruitful discussions and Vincent Guidard for the 4DVar ARPEGE-SH configuration.

This is a contribution to the Year of Polar Prediction (YOPP), a flagship activity of the Polar Prediction Project (PPP), initiated by the World Weather Research Programme (WWRP) of the World Meteorological Organisation (WMO). We acknowledge the WMO WWRP for its role in coordinating this international research activity.

Data used in this manuscript was produced as part of the international Multidisciplinary drifting Observatory for the Study of the Arctic Climate (MOSAiC) with the tag MOSAiC20192020 and Polarstern expedition AWI_PS122_00.

This study was partly funded by the H2020-APPLICATE project, EU grant number 727862.

## References

• Salias y Mélia D., 2002 : A global coupled sea ice-ocean model. Ocean Modelling 4, 137-172..

• Voldoire A., et al. "Evaluation of CMIP6 DECK Experiments With CNRM-CM6-1." Journal of Advances in Modeling Earth Systems 11.7 (2019): 2177-2213.

# Investigations of the International Experiments, GAME and I-STEP and the Global Atmospheric Model Findings

**Z.N. Begum**

Ex-Scientist 'G'/Adviser, Department of Science and Technology, New Delhi, India.
OWSD Full Member, ICTP, Trieste, Italy.

The investigations and the findings presented in this paper may provide some research insight, which is relevant to the atmospheric-environmental findings of Global Atmospheric Models vis-à-vis GAME (GEWEX) and I-STEP Programmes, where GEWEX is the abbreviation for the 'Global Energy and Water Cycle Experiment'. The observations under these programmes will not only improve our understanding but also will help us to improve the representation of these processes in the "atmospheric general circulation model" [AGCM(O)], which is basically the Global Spectral Model T80. It is originally adapted from NCEP, NMC, USA (Kanamitsu,1989). Its important features are model dynamics and modifications made in the model physics (Begum, 2003; Begum, 2005; Begum, 2017; George and Begum, 1997), which we call as [AGCM(M)], where M refers to "modified". As the main objective of GAME is to understand the role of Asian monsoon in the global energy budget and water cycle, in the present experiment we have computed the hydrological budget (Fig.1). The experimental model shows reasonable balance between the evaporation and precipitation.

The GEWEX data and assessment panel guide the long-term global atmospheric surface water and energy budget products. Use of such experiments help in developing and improving representation of the atmosphere in weather and climate models. A related experiment, GAME (Global Asian Monsoon Experiment) is also implemented to understand the role of the Asian monsoon in the global energy and water cycle.

The I-STEP is the 'International Solar-Terrestrial Energy Programme', which is the key parameter ISTEP programme. It combines resources on an International level, determining the flow of mass, momentum and energy in the solar-terrestrial environment.

These investigations provide some research insight of the model predictions and its role in understanding atmospheric-environmental findings of GEWEX and I-STEP programmes.

## References

1. Begum, Z.N. (2003), *A theoretical investigation of the radiative effects and microphysical processes involved in the interaction of aerosol particulates in the atmosphere and validation of the theoretical results with the INDOEX observations*; JQSRT, 78, 99-103.
2. Begum, Z.N. (2005), *Modeling of chemical tracer transport in the atmospheric environment and its impact on the global climate*; JQSRT, 95, 423-7.

3. Begum, Z.N. (2017), *The effect of radiative forcing of various constituents of earth atmosphere on the global energy transfer*; WCRP Report No. 12/2017 on "World Climate Research Programme – Research Activities in Atmospheric and Ocean Modeling, Section 4.

4. George, J.P., Begum, Z.N. (1997), Atmosfera, 10, 1-22.

5. Kanamitsu, M. (1989), Weather Forecasting, 4, 335-42.

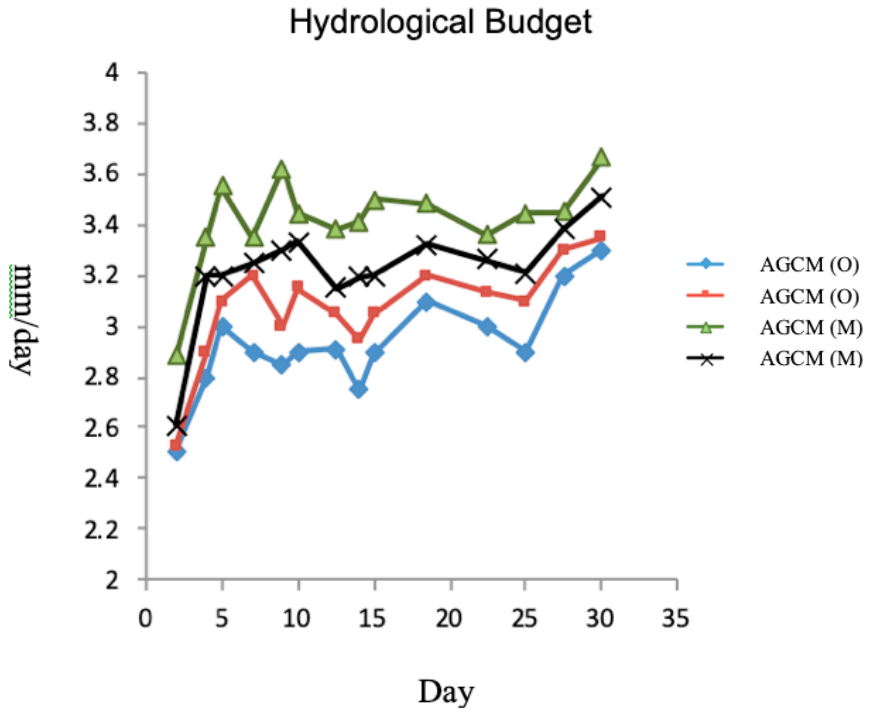


**Fig. 1.** Total precipitation and surface evaporation over the globe for 30 days integration of June 1995, 00z initial condition by the AGCM original model [AGCM(O)] and the modified model [AGCM(M)].

# Preliminary Evaluation of NOAA's GEFS-Aerosol Model

Partha S. Bhattacharjee[1], Li Pan[1], B.Baker[2], K. Zhang[3], R. Montuoro[3], G. Grell[4], S. McKeen[5], J.T.McQueen[6]

*[1]IMSG-College Park, MD, [2]ARL-College Park, MD, [3]CIRES Univ. of Colorado, [4]GSD ESRL NOAA-Boulder, CO, [5]CSL ESRL, NOAA-Boulder, CO, [6]NWS/NCEP/EMC-College Park, MD*

Email: jeff.mcqueen@noaa.gov

The National Centers for Environmental Prediction (NCEP) has partnered with NOAA/ESRL Global Systems Laboratory (GSL), Chemical Sciences Laboratory (CSL), NOAA/OAR Air Resources Lab (ARL), the NOAA/NESDIS Center for Satellite Applications and Research (STAR) and NASA Goddard Space Flight Center to develop a global aerosol model that will replace the current NEMS GFS Aerosol Component (NGAC) (Wang et al., 2018). The new model will be a single member named GEFS-Aerosol in Version 12 of the Global Ensemble Forecast System (GEFS). The meteorology of this new model is based on the operational Global Forecast System (GFS v15) and most of the aerosol modules are from the Goddard Chemistry Aerosol Radiation and Transport (GOCART) (Colarco et al., 2010). Recent updates and additions include the biomass burning plume rise module added from WRF-Chem; tracer convective transport and wet scavenging implemented in the Simplified Arakawa-Schubert (SAS) convection scheme; the FENGSHA dust scheme implemented and developed by ARL (Dong et al., 2016); biomass-burning emission calculations based on the Blended Global Biomass Burning Emissions Product (GBBEPx V3) emission, and Fire Radiative Power (FRP) data provided by NESDIS (Zhang et al., 2012). Once implemented operationally, GEFS-Aerosol will provide a 5-day forecast of total aerosol as well as component dust, organic and biomass carbon, sea-salt and sulfate aerosol at a global horizontal resolution of ~0.25 by 0.25 degrees, and 4 times per day (at 00, 06, 12 and 18 Coordinated Universal Time (UTC). It will also provide Particulate Matter (PM 2.5 & PM10) forecasts along with 3-dimensional mixing ratios of aerosol species at 64 model vertical levels.

A nearly one-year retrospective run has been conducted using GEFS-Aerosol to provide multi-species forecasts of Aerosol Optical Depth (AOD) and other aerosol properties. AOD observation from satellites, International Cooperative for Aerosol Prediction Multi-Model Ensemble (ICAP-MME) and reanalysis from NASA MERRA2-Aerosol are used to extensively evaluate model results. Figure 1 shows daily day-1 AOD forecasts at the 550-nm wavelength from GEFS-Aerosol compared against operational NGACv2 and MERRA2 over different global aerosol regions. The results show that GEFS-Aerosol has made remarkable improvement across all aerosol regimes compared to NGACv2. Over North Africa dust AOD dominates (from the Sahara dust source region and downwind sides) in the boreal summer, whereas the Amazon forest fire season starts from late August. Both natural and anthropogenic aerosols contribute to the other three regions in the figure. GEFS-Aerosol has shown improvement in model forecasts and in reducing forecast bias over biomass burning areas and over some of the anthropogenic aerosol dominated regions (mainly over India, Southeast Asia and East Asia).

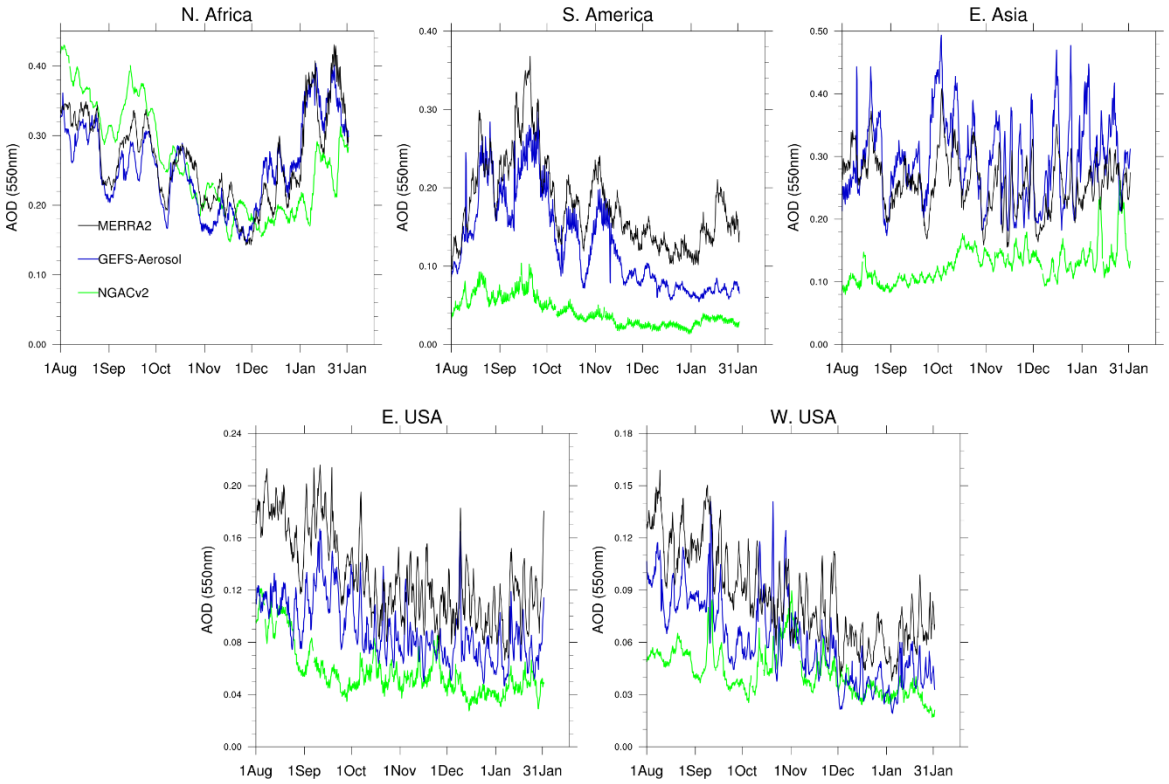


**Figure 1.** Daily day-1 GEFS-Aerosol model forecasts over five global regions compared against NGACv2 and MERRA2-reanalysis for six months between August 2019 and January, 2020. Latitude and longitude bounds to compute area averages are North Africa (0°-35°N, 18°W-30°E), South America (0°-35°S, 35°-80°W), East Asia (20°-48°N, 100°-140°E), Eastern USA (25°-48°N, 68°-95°W) and Western USA (25°- 48°N, 95°-125°W).

## References

Colarco, P., A. da Silva, M. Chin, and T. Diehl, 2010. Online simulations of global aerosol distributions in the NASA GEOS-4 model and comparisons to satellite and ground-based aerosol optical depth, J. Geophy. Res., 115, D14207, doi: 10.1029/2009JD012820.

Dong, X., J. S. Fu, K. Huang, D. Tong, and G. Zhuang, 2016: Model development of dust emission and heterogeneous chemistry within the Community Multiscale Air Quality modeling sys-tem and its application over East Asia. Atmos. Chem. Phys.,16, 8157–8180, doi:10.5194/acp-16-8157-2016.

Wang, J. et al., 2018. The implementation of NEMS GFS Aerosol Component (NGAC) Version 2.0 for global multispecies forecasting at NOAA/NCEP – Part 1: Model descriptions, Geosci. Model Dev., 11, 2315–2332, https://doi.org/10.5194/gmd-11-2315-2018.

Zhang, X., S. Kondragunta, J. Ram, C. Schmidt, and H-C Huang, 2012. Near-real-time global biomass burning emissions products from geostationary satellite constellation, J. Geophys. Res., 117, D14201, doi:10.1029/2012JD017459.

# Climate anomalies in the North Eurasian regions: predictability for different El-Nino conditions

I.I. Mokhov[1,2] and A.V. Timazhev[1]

[1]A.M. Obukhov Institute of Atmospheric Physics RAS
[2]Lomonosov Moscow State University
mokhov@ifaran.ru

The impact of the El-Niño/La-Niña events is significant on a global scale, including North Eurasian regions [2]. In [3] estimates of possible anomalies in Russian regions in 2016 in May-July are obtained, taking into account the beginning of the year in the El-Niño phase and the forecasts of its transformation by the end of the year. Here we present similar estimations for 2020 with the beginning in the neutral phase of canonical El-Nino characterized by Nino3 index (Eastern Pacific El-Nino). At the same time the beginning of this year was in the El-Nino phase of El-Nino characterized by Nino4 index (Central Pacific El-Nino). The El-Niño (*E*), La-Niña (*L*) and neutral (*N*) phases are defined similar to [2].

According to model predictive estimates (https://www.cpc.ncep.noaa.gov/) obtained by the beginning of May 2020 using the Nino 3.4 index, during 2020 the probability of the continuation of the neutral phase decreases, the La Niña phase increases and the probability of the El Nino phase remains low (about 10%). At the same time, by the end of 2020, the probabilities of the *N*-phase and *L*-phase are comparable (more than 40%), and by the beginning of 2021, the probability of the *L*-phase is slightly higher than the *N*-phase.

We analyzed the spring-summer (May-June-July) anomalies of surface air temperature (SAT) $\delta T$ for European (ER) and Asian (AR) parts of Russia in mid-latitudes from observations since 1891 [1] (see also [3]). Tables 1a,b show the estimates for probability of spring–summer SAT anomalies $\delta T$ in May-June-July for ER and AR (in brackets) for different transitions from the *N* and *E* phases at the beginning of the year with the use Nino 3 (a) and Nino 4 (b) indices from observations since 1891.

Table 1a. Probability of positive and negative surface air temperature anomalies ($\delta T$) in the ER (and AR) in May-July for different ENSO phase transitions (characterized by the Niño3 index) from observations since 1891 for ER and AR (in brackets).

| ***δT*, K** | | ***Nino 3*** | | | | | |
|---|---|---|---|---|---|---|---|
| | | ***N→E*** *n*=18 | ***N→L*** *n=11* | ***N→N*** *n=39* | ***E→E*** *n*=4 | ***E→L*** *n*=9 | ***E→N*** *n*=15 |
| >0 | >0 | 0.44 (0.50) | 0.64 (0.45) | 0.62 (0.62) | 0.75 (0.50) | 0.89 (0.44) | 0.40 (0.40) |
| | >1K | 0.17 (0.22) | 0.18 (0.09) | 0.31 (0.31) | 0.25 (0.50) | 0.56 (0.11) | 0.13 (0.27) |
| ≤0 | ≤0 | 0.56 (0.50) | 0.36 (0.55) | 0.38 (0.38) | 0.25 (0.50) | 0.11 (0.56) | 0.60 (0.60) |
| | ≤-1K | 0.22 (0.06) | 0.18 (0) | 0.13 (0.10) | 0 (0.25) | 0 (0.22) | 0.33 (0.27) |

According to the values of the Nino3 index, 2020 began in the neutral phase. At the most probable phase transitions *N→L* and *N→N*, the probability of a positive temperature anomaly for EP in May-July is noticeably (more than one and a half times) greater than negative. For AR, the probabilities of positive and negative anomalies differ significantly for the *N→L* and *N→N* phase transitions. The highest probability of extreme temperature anomalies was estimated for the *N→N* transition with a probability for positive temperature anomalies in EP and AR (more than 30%) more than twice those for the negative ones.

Table 1b. Probability of positive and negative surface air temperature anomalies (δ*T*) in the ER (and AR) in May-July for different ENSO phase transitions (characterized by the Niño4 index) from observations since 1891 for ER and AR (in brackets).

| ***δT*, K** | | ***Nino 4*** | | | | | |
|---|---|---|---|---|---|---|---|
| | | ***N→E*** *n*=18 | ***N→L*** *n=9* | ***N→N*** *n=41* | ***E→E*** *n*=8 | ***E→L*** *n*=8 | ***E→N*** *n*=13 |
| >0 | >0 | 0.44 (0.44) | 0.56 (0.44) | 0.63 (0.61) | 0.38 (**0.75**) | **0.88** (0.63) | 0.54 (0.38) |
| | >1K | 0.17 (0.22) | 0.22 (0.11) | 0.22 (0.22) | 0.25 (**0.75**) | **0.50** (0.13) | 0.31 (0.15) |
| ≤0 | ≤0 | 0.56 (0.56) | 0.44 (0.56) | 0.37 (0.39) | **0.63** (0.25) | 0.13 (0.38) | 0.46 (**0.62**) |
| | ≤-1K | 0.17 (0.17) | 0.11 (0) | 0.17 (0.12) | **0.38** (1/8) | 0 (0.13) | 0.31 (0.23) |

According to the Nino 4 index, the year 2020 began in the *E*-phase. At the most probable phase transitions *E→L* and *E→N*, the probability of a positive temperature anomaly for EP in May-July, as with the Nino3 index, is greater than negative. With 8 analyzed most probable phase transitions *E→L*, positive cases were observed in 7 cases, and extreme positive temperature anomalies in 4 cases in May-July for EP. For AR, the probabilities of positive and negative anomalies differ significantly for the phase transitions *E→L* and *E→N*.

This work was supported by the RSF (project No. 19-17-00240). Analysis for North Asia regions was carried out in the framework of the RFBR project (17–29–05098).

**References**

Meshcherskaya A.V., Mirvis V.M., Golod M.P. The drought in 2010 against the background of multiannual changes in aridity in the major grain-producing regions of the European part of Russia. *Tr. MGO,* 2011, **563**, 94–121 (in Russian)

Mokhov I.I., Timazhev A.V. Drought risk in the North Eurasian regions: Assessment of El-Nino effects. *Res. Activ. Atmos. Ocean. Modell.* E. Astakhova (ed.). WCRP Rep. No.12/2015, 2015, 2.6–2.7.

Mokhov I.I., Timazhev A.V. Weather-climate anomalies in Russian regions: El Niño-associated predictability. *Res. Activ. Atmos. Ocean. Modell*. E. Astakhova (ed.). WCRP Rep. No.15/2016, 2016, 6.9–6.10.

**Warm and cold winters in the North Eurasian regions: Assessment of El-Niño effects**

I.I. Mokhov[1,2]
[1]A.M. Obukhov Institute of Atmospheric Physics RAS
[2]Lomonosov Moscow State University
mokhov@ifaran.ru

The probability of warm and cold winters, in particular extremely warm and very cold winters, in the regions of Northern Eurasia is estimated for different phases of El-Nino. Monthly-mean data for surface temperature anomalies (SAT) $\delta T$ in January and February for the period 1936-2014 from [1] for different regions are used. In particular, the ratio of δT for January and February to the standard deviation $\sigma T$ for the period 1961-1990 (index $\alpha = \delta T/\sigma T$) was used for different regions. Winters range from extremely warm (EWW) and extremely cold (ECW) to considerably warm (CWW) and considerably cold (CCW), as well as moderately warm (MWW) and moderately cold (MCW) winters.

Table 1 (a, b, c) presents the number and probability estimates of warm and cold winters for ETR (a), Baikal and Transbaikalia (b) and Amur and Primorye (c) south of 60ºN during the onset of various El-Nino phases, characterized by Nino3 and Nino4 indices. The largest total number of cold and warm winters is characteristic for neutral (*N*) phases of El-Niño for all considered regions. This is due to the fact that the total number of years in the *N*-phase is greater than the total number of years in the El-Nino (*E*) and La-Nina (*L*) phases. Estimates of the probability of an abnormal winter for the expected *E*-phase or *L*-phase can be significantly higher than the corresponding estimates for the *N*-phase. For example, the probability of a warm winter for ETR is estimated to be the highest in the *E*-phase (more than 2/3), and the probability of a cold winter is estimated as the highest in the *L*-phase.

Table 1a.

| 1936-2014 | | (a) European region | | | | | | | |
|---|---|---|---|---|---|---|---|---|---|
| | | Warm Winters | | | | Cold Winters | | | |
| | | *EWW* | *CWW* | *MWW* | ∑ | *ECW* | *CCW* | *MCW* | ∑ |
| Nino3 | *N* $n_\Sigma$=44 | 4 (0.09) | 10 (0.23) | 11 (0.25) | 25 (0.57) | 5 (0.11) | 6 (0.14) | 8 (0.18) | 19 (0.43) |
| | *L* $n_\Sigma$=19 | 3 (0.16) | 4 (0.21) | 2 (0.11) | 9 (0.47) | 3 (0.16) | 4 (0.21) | 3 (0.16) | 10 (0.53) |
| | *E* $n_\Sigma$=16 | 1 (0.06) | 4 (0.25) | 6 (0.38) | 11 (0.69) | 0 (0) | 1 (0.06) | 4 (0.25) | 5 (0.31) |
| Nino4 | *N* $n_\Sigma$=40 | 3 (0.08) | 10 (0.25) | 8 (0.20) | 21 (0.53) | 3 (0.08) | 6 (0.15) | 10 (0.25) | 19 (0.48) |
| | *L* $n_\Sigma$=18 | 3 (0.17) | 4 (0.22) | 2 (0.11) | 9 (0.50) | 3 (0.17) | 4 (0.22) | 2 (0.11) | 9 (0.50) |
| | *E* $n_\Sigma$=21 | 2 (0.10) | 4 (0.19) | 9 (0.43) | 15 (0.71) | 2 (0.10) | 1 (0.05) | 3 (0.14) | 6 (0.29) |

The greatest probability of warm winters for ETR in years starting in the *E*-phase is mainly associated with MWW. Estimates of the MWW probabilities for ETR in the *E*-phase are up to two or more times greater than in other phases. At the same time the estimates of the number and probability of cold winters for ETR are minimal in the *E*-phase, and the number and probability estimates of warm winters are in the *L*-phase. The lowest values of the cold winter probability for ETR are estimated for the *E*-phase. The probability of warm winters for ETR is estimated to be maximum in the E-phase and this is mainly due to MWW.

Table1b.

| 1936-2014 | | (b) Baikal Lake region | | | | | | | |
|---|---|---|---|---|---|---|---|---|---|
| | | Warm Winters | | | | Cold Winters | | | |
| | | *EWW* | *CWW* | *MWW* | ∑ | *ECW* | *CCW* | *MCW* | ∑ |
| Nino3 | *N* $n_\Sigma$=44 | 4 (0.09) | 13 (0.30) | 5 (0.11) | 22 (0.50) | 5 (0.11) | 6 (0.14) | 11 (0.25) | 22 (0.50) |
| | *L* $n_\Sigma$=19 | 4 (0.21) | 4 (0.21) | 3 (0.16) | 11 (0.58) | 0 (0) | 0 (0) | 8 (0.42) | 8 (0.42) |
| | *E* $n_\Sigma$=16 | 0 (0) | 1 (0.06) | 3 (0.19) | 4 (0.25) | 3 (0.19) | 5 (0.31) | 4 (0.25) | 12 (0.75) |
| Nino4 | *N* $n_\Sigma$=40 | 3 (0.08) | 10 (0.25) | 3 (0.08) | 16 (0.40) | 7 (0.18) | 5 (0.13) | 11 (0.28) | 23 (0.58) |
| | *L* $n_\Sigma$=18 | 3 (0.17) | 5 (0.28) | 4 (0.22) | 12 (0.67) | 0 (0) | 0 (0) | 6 (0.33) | 6 (0.33) |
| | *E* $n_\Sigma$=21 | 2 (0.10) | 3 (0.14) | 4 (0.19) | 9 (0.43) | 1 (0.05) | 6 (0.29) | 6 (0.29) | 13 (0.62) |

The probability of warm winters for Pribaikalye and Transbaikalia is usually higher in the *L*-phase, and the probability of cold winters is estimated as the highest in the *E*-phase (up to ¾). The number and probability estimates of cold winters in the Baikal and Transbaikalia regions are minimal in the *L*-phase, and the number of warm winters in the *E*-phase. It should be noted that in 24 years with ECW and CCW such winters were never observed in this region in the *L*-phase.

Table 1c.

| 1936-2014 | | (c) Amur River region | | | | | | | |
|---|---|---|---|---|---|---|---|---|---|
| | | Warm Winters | | | | Cold Winters | | | |
| | | *EWW* | *CWW* | *MWW* | ∑ | *ECW* | *CCW* | *MCW* | ∑ |
| Nino3 | *N* $n_\Sigma$=44 | 5 (0.11) | 8 (0.18) | 9 (0.20) | 22 (0.50) | 4 (0.09) | 7 (0.16) | 11 (0.25) | 22 (0.50) |
| | *L* $n_\Sigma$=19 | 2 (0.11) | 8 (0.42) | 1 (0.05) | 11 (0.58) | 1 (0.05) | 2 (0.11) | 5 (0.26) | 8 (0.42) |
| | *E* $n_\Sigma$=16 | 1 (0.06) | 2 (0.13) | 4 (0.25) | 7 (0.44) | 3 (0.19) | 2 (0.13) | 4 (0.25) | 9 (0.56) |
| Nino4 | *N* $n_\Sigma$=40 | 3 (0.08) | 7 (0.18) | 7 (0.18) | 17 (0.43) | 2 (0.05) | 8 (0.20) | 13 (0.33) | 23 (0.58) |
| | *L* $n_\Sigma$=18 | 2 (0.11) | 7 (0.39) | 2 (0.11) | 11 (0.61) | 2 (0.11) | 1 (0.06) | 4 (0.22) | 7 (0.39) |
| | *E* $n_\Sigma$=21 | 3 (0.14) | 4 (0.19) | 5 (0.24) | 12 (0.57) | 4 (0.19) | 2 (0.10) | 3 (0.14) | 9 (0.43) |

It is worth to note, that the probability of a warm winter in the Amur Region and Primorye at El Niño with positive anomalies of equatorial SST in the central Pacific Ocean is estimated to be 30% higher than with positive anomalies in the eastern Pacific Ocean, and the corresponding probability of a cold winter - on the contrary - by 30% less.

This work was supported by the RSF (project No. 19-17-00240). Analysis for North Asia regions was carried out in the framework of the RFBR project (17–29–05098).

## References

1. Mescherskaya A.V., Golod M.P. (2015) Catalogs of abnormal winters over the Russian territory. *Proc. MGO*, **579**, 130−162. (in Russian)

# Effects of stratospheric volcanic aerosols on S2S prediction skill

OTSUKA Natsuko[1,*], SEKIGUCHI Ryohei[1], KOMORI Takuya[1] and TANAKA Taichu[2]

1. Climate Prediction Division, Japan Meteorological Agency, Tokyo, Japan
2. Meteorological Research Institute, Japan Meteorological Agency, Tsukuba, Japan
Email: n-otsuka@met.kishou.go.jp

## 1. Introduction

Volcanic eruptions significantly affect climate prediction due to related dispersion of aerosols that remain in the stratosphere for years (McCormic et al. 1995, Zambri et al. 2019). Stratospheric volcanic aerosols are generally produced by chemical reaction from gaseous sulfur dioxide ($SO_2$) to sulfuric acid ($H_2SO_4$) particles, and result in increased reflection of solar radiation back into space due to a higher Earth albedo along with absorption of upwelling infrared radiation. Therefore, stratosphere can be warmed by both radiation effects, while the troposphere can be cooled by solar radiation effect.

In light of the link between weather and climate predictions, volcanic aerosols can be considered to potentially influence skill in tropospheric temperature prediction on a sub-seasonal to seasonal (S2S) timescale. Accordingly, this study involved a revision of the radiation scheme in a case of the Mt. Pinatubo eruption with focus on radiative heating and resulting temperature changes due to volcanic aerosols in S2S prediction.

## 2. Experimental design with a revised radiation scheme

The Japan Meteorological Agency (JMA) is developing the next-generation Coupled Seasonal Ensemble Prediction System Version 3 (JMA/MRI-CPS3; CPS3), which consists of 60km atmospheric and eddy-permitting (0.25 deg.) ocean components. The current radiation scheme in CPS3 can deal with the direct effects of aerosols categorized into 5 types (sulfate, organics, black carbon, sea salt and dust) input as monthly climatological forcing data (JMA, 2019), but also needs to be able to handle stratospheric volcanic aerosols. The optical properties of such aerosols are determined via Mie scattering calculation, in which size distribution parameters and complex refractive indices are obtained from the OPAC database (Hess et al., 1998) for stratospheric sulfate droplets. The volcanic stratospheric aerosol information for the scheme is given as external monthly data as developed for CCMI-1 and CMIP6 (Revell et al., 2017). Monthly climatological tropospheric aerosols are pre-computed using JMA's MASINGAR global aerosol model (Tanaka et al. 2003). By May 1992, a year after the eruption of Mt. Pinatubo in the Philippines, volcanic aerosols were observed worldwide in the stratosphere (Figure 1). To verify prediction skill with the revised radiation scheme in this case, 13-member ensemble forecasting was conducted using CPS3.

## 3. Results

Results from a six-month forecast experiment (TEST) with an initial time of 00 UTC on 26 April 1992 using the revised radiation scheme were compared to those of a control experiment (CNTL) based on CPS3 configuration. As expected, due to the effects of stratospheric volcanic aerosols, both solar and infrared radiation caused stratospheric warming, while tropospheric cooling was calculated in relation to solar radiation (Figure 2).

The temperature difference on the S2S timescale was demonstrated in a six-month forecast experiment. Heating-rate differences of solar and infrared radiations make a stable condition with less heating rate of vertical diffusion in the lower troposphere, causing inactive deep convection and less cloud amount in the upper troposphere over the tropics (not shown). As a result, stratospheric temperatures increased and tropospheric temperatures decreased globally (Figure 3). Verification results against ERA5 reanalysis (Hersbach et al., 2020) show that TEST outperformed CNTL in temperature biases in the stratosphere and lower troposphere, although there is still room for improvement in the upper troposphere depending on the characteristics of physics in CPS3 (Figure 4). Overall, the revision of the radiation scheme shows encouraging and promising results for many aspects due to the stratospheric volcanic aerosols.

## Reference

Hersbach, H., B.Bell, P. Berrisford, S. Hirahara, András Horányi1, J. Muñoz-Sabater, J. Nicolas, C. Peubey, R. Radu, D. Schepers, A. Simmons, C. Soci, S. Abdalla, X. Abellan, G. Balsamo, P. Bechtold, G. Biavati, J. Bidlot, M. Bonavita, G. De Chiara1, P. Dahlgren, D. Dee, M. Diamantakis, R. Dragani, J. Flemming, R. Forbes, M. Fuentes, A. Geer, L. Haimberger, S. Healy, R.J. Hogan1, E. Hólm, M. Janisková, S. Keeley, P. Laloyaux, P. Lopez, G. Radnoti, P. de Rosnay, I. Rozum, F. Vamborg, S. Villaume and J.-N. Thépaut, 2020: The ERA5 Global Reanalysis. Submitted to *Q. J. R. Meteorol. Soc.*

Hess, M., P. Koepke, and I. Schult, 1998: Optical properties of aerosols and clouds: The software package OPAC. *Bull. Amer. Meteor. Soc.*, 79, 831-844.

McCormic, M. P., L. W. Thomason, and C. R. Trepte, 1995: Atmospheric effects of the Mt Pinatubo eruption, *Nature*, 373, 399–404.

JMA, 2019: Outline of the operational numerical weather prediction at the Japan Meteorological Agency. Appendix to WMO technical progress report on the global data-processing and forecasting system and numerical weather prediction research. 188pp. Available online:
http://www.jma.go.jp/jma/jma-eng/jma-center/nwp/outline2019-nwp/index.htm

Revell, L. E., Stenke, A., Luo, B., Kremser, S., Rozanov, E., Sukhodolov, T., and Peter, T., 2017: Impacts of Mt Pinatubo volcanic aerosol on the tropical stratosphere in chemistry–climate model simulations using CCMI and CMIP6 stratospheric aerosol data, *Atmos. Chem. Phys.*, **17**, 13139-13150, doi:10.5194/acp-17-13139-2017.

Tanaka, T. Y., K. Orito, T. T. Sekiyama, K. Shibata, M. Chiba, and H. Tanaka, 2003: MASINGAR, a global tropospheric aerosol chemical transport model coupled with MRI/JMA98 GCM: Model description. *Papers in Meteorology and Geophysics*, 53(4), 119-138.

Zambri, B., A. Robock, M. J. Mills, and A. Schmidt, 2019: Modeling the 1783–1784 Laki Eruption in Iceland, Part II: Climate Impacts, *J. Geophys. Res.*, 124(13), 6770-6990.

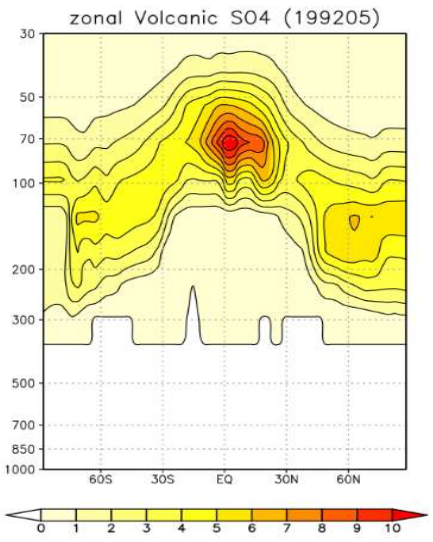


**Figure 1.** Zonal mean of volcanic aerosols [S mg/m2], averaged for May 1992.

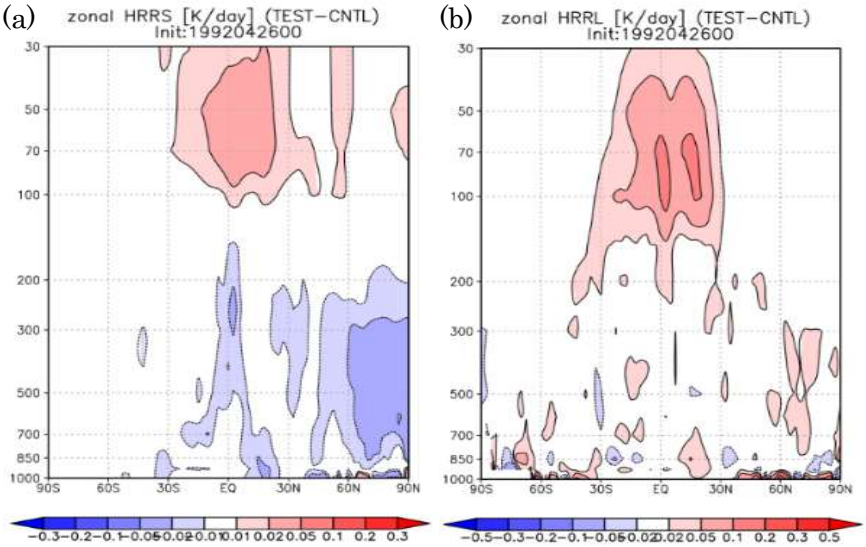


**Figure 2.** Zonal mean of heating rate differences [K/day] (TEST minus CNTL) of 13-member averaged (a) solar and (b) infrared radiation averaged over one month forecasts with an initial time of 00 UTC on 26 April 1992.

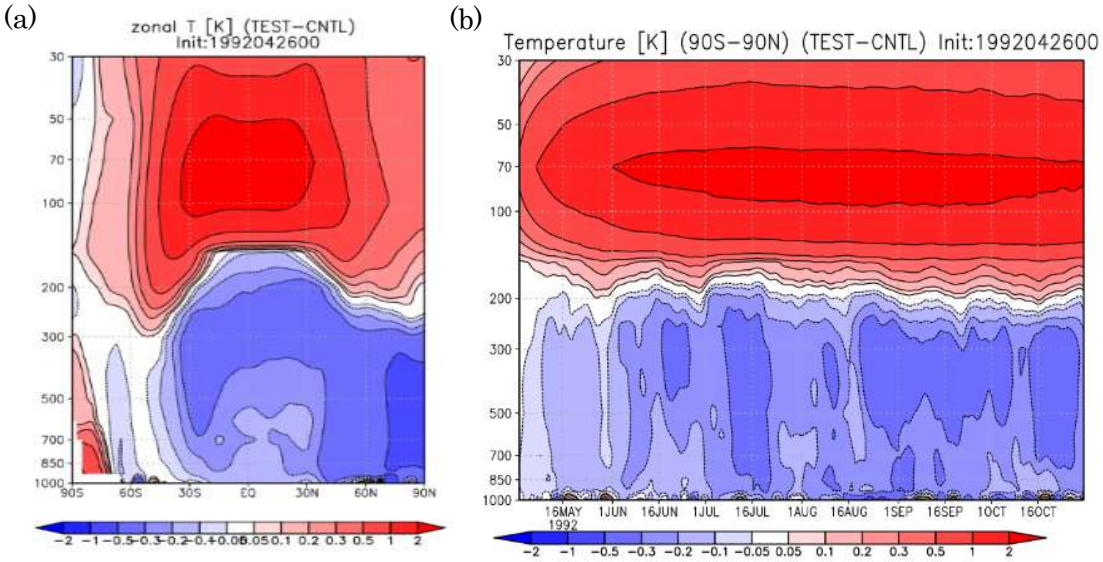


**Figure 3.** 13-member average temperature differences [K] (TEST minus CNTL) with (a) zonal mean and (b) pressure-time cross section of the global mean over six-month forecasting with an initial time of 00 UTC on 26 April 1992.

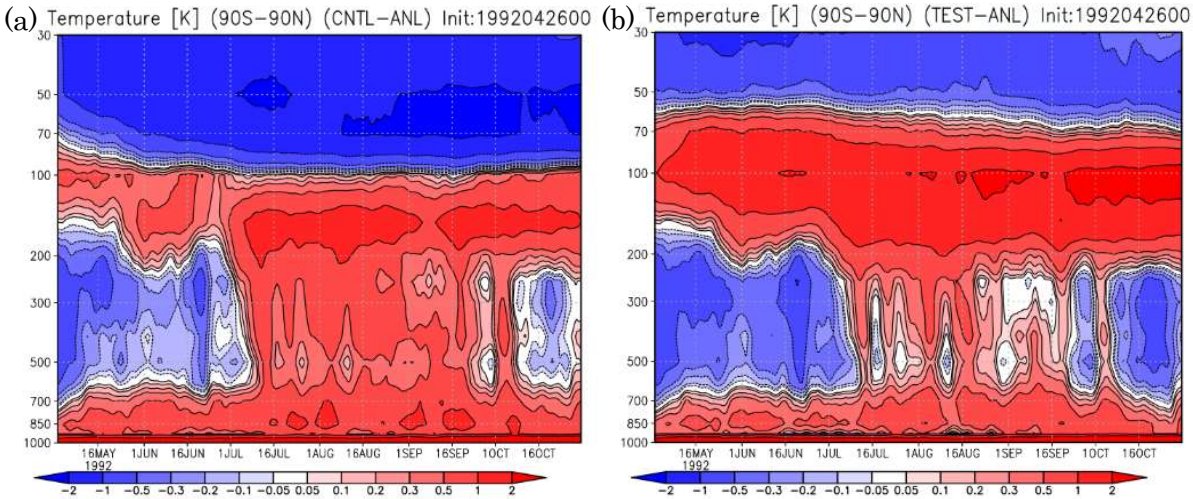


**Figure 4.** 13-member average pressure-time cross section of global average temperature errors [K] against ERA5 reanalysis for (a) CNTL and (b) TEST over six-month forecasting with an initial time at 00 UTC on 26th April 1992.

# Two-tiered sea surface temperature approach implemented to JMA's Global Ensemble Prediction System

TAKAKURA Toshinari* and KOMORI Takuya
Climate Prediction Division, Japan Meteorological Agency, Tokyo, Japan
E-mail: t-takakura@met.kishou.go.jp

## 1. Introduction

The Japan Meteorological Agency (JMA) operates the Global Ensemble Prediction System (GEPS) to support issuance of operational typhoon information as well as one-week, two-week and one-month forecasts. Sea surface temperature (SST) is recognized as an important variable in forecasting on subseasonal to seasonal scales, and the SST data used in this system are prescribed as persisting anomalies from the climatological SST throughout the forecast period. The SST configuration can potentially cause large errors in forecasts over weeks 3 and 4. To tackle this issue with limited computational cost, a two-tiered SST approach was applied for the GEPS lower-boundary condition to force the atmospheric model with more realistic SST data. Specifically, the lower boundary condition of the atmospheric model in the tropics and subtropics was relaxed from anomaly-fixed SST to operationally precomputed SST by the seasonal EPS, and the approach was evaluated via 30-year reforecast experiments.

## 2. Experimental design

The specifications of the reforecast experiments were as per Sekiguchi et al. (2018), except the ensemble size was 13 and the initial dates were only for the end of the month from 1981 to 2010. In the CNTL experiment, the model was forced using anomaly-fixed SST as a lower boundary condition. A two-tiered SST approach (e.g., Zhu et al. 2018) was applied in the TEST experiment, and the lower boundary condition was relaxed from anomaly-fixed SST to the ensemble mean SST of JMA's seasonal EPS (JMA/MRI-CPS2: JMA/Meteorological Research Institute-Coupled Prediction System version 2; Takaya et al. 2018) reforecast data. The SSTs were as per CNTL for the first 11 days, and the relaxation was introduced linearly from day 12 to day 18 exclusively to the tropics and subtropics, since comparison suggests that higher-latitude SSTs are still better prescribed using fixed anomalies.

## 3. Results

Figure 1 shows the anomaly correlation coefficient (ACC) averaged for all initial dates over weeks 3 and 4. The ACC of surface temperature showed particular improvement for the area over the Indian Ocean and the Asian monsoon region. Since SSTs in these regions vary on a subseasonal time scale, the accuracy of anomaly-fixed SST data exhibits a significant decreasing tendency. Improvement is also observed for the ACC of the 200-hPa stream function and velocity potential over the Indian Ocean and the Asian monsoon region. Although the two-tiered SST approach was applied only to the tropics and the subtropics, these positive effects in the upper level extend to the mid-latitudes. Madden-Julian Oscillation (MJO) forecast skill was also improved in the latter period of the forecast. Specifically, the correlation of the MJO index (Matsueda and Endo, 2011) was improved by 0.1 over weeks 3 and 4 (Figure 2) due to reduced phase error. However, amplitude error increased slightly because forecast activity tended to degrade in relation to the use of relatively coarse SSTs from the seasonal EPS (not shown).

The relationship between SST and precipitation was closer to that of analysis with application of the two-tiered SST approach. The correlation in analysis shows negative values for the area over the Western Pacific region, but was strongly positive in the CNTL experiment due to a lack of cloud-shortwave radiation-SST feedback (Figure 3). Overly enhanced convective activity is in fact a known issue in the GEPS. The correlation in the TEST experiment was positive but better than that of the CNTL experiment because the precomputed SST indirectly incorporates negative feedback effects.

## References

Huffman, G.J., R.F. Adler, M. Morrissey, D.T. Bolvin, S. Curtis, R. Joyce, B. McGavock, and J. Susskind, 2001: Global precipitation at one-degree daily resolution from multisatellite observations. *J. Hydrometeor*., **2**, 36-50.

Kurihara, Y., T. Sakurai, and T. Kuragano, 2006: Daily sea-surface temperature over the global ocean constructed from satellite microwave, infrared and in-situ observations. *JMA Sokkoujihou special issue*, **73**, S1−S18 (in Japanese).

Matsueda, M., and H. Endo, 2011: Verification of medium-range MJO forecasts with TIGGE. *Geophys. Res. Lett*., **38**, L11801.

Sekiguchi, R., Y. Adachi, T. Kanehama, Y. Kubo, K. Miyaoka, A. Nishimura, A. Shimpo, T. Yoshida, 2018: Verification of JMA's new GEPS for one-month prediction. *CAS/JSC WGNE Res. Activ. Atmos. Oceanic Modell.*, **48**, 6.11-6.12.

Takaya, Y., S. Hirahara, T. Yasuda, S. Matsueda, T. Toyoda, Y. Fujii, H. Sugimoto, C. Matsukawa, I. Ishikawa, H. Mori, R. Nagasawa, Y. Kubo, N. Adachi, G. Yamanaka, T. Kuragano, A. Shimpo, S. Maeda and T. Ose, 2018: Japan Meteorological Agency/Meteorological Research Institute-Coupled Prediction System version 2 (JMA/MRI-CPS2): atmosphere-land-ocean-sea ice coupled prediction system for operational seasonal forecasting. *Clim. Dyn*., **3-4**, 751-765, doi:10.1007/s00382-017-3638-5.

Zhu, Y., X. Zhou, W. Li, D. Hou, C. Melhauser, E. Sinsky, M. Peña, B. Fu, H. Guan, W. Kolczynski, R. Wobus, and V. Tallapragada, 2018: Toward the improvement of subseasonal prediction in the National Centers for Environmental Prediction Global Ensemble Forecast System. *J. Geophys. Res.: Atmospheres*, **123**.

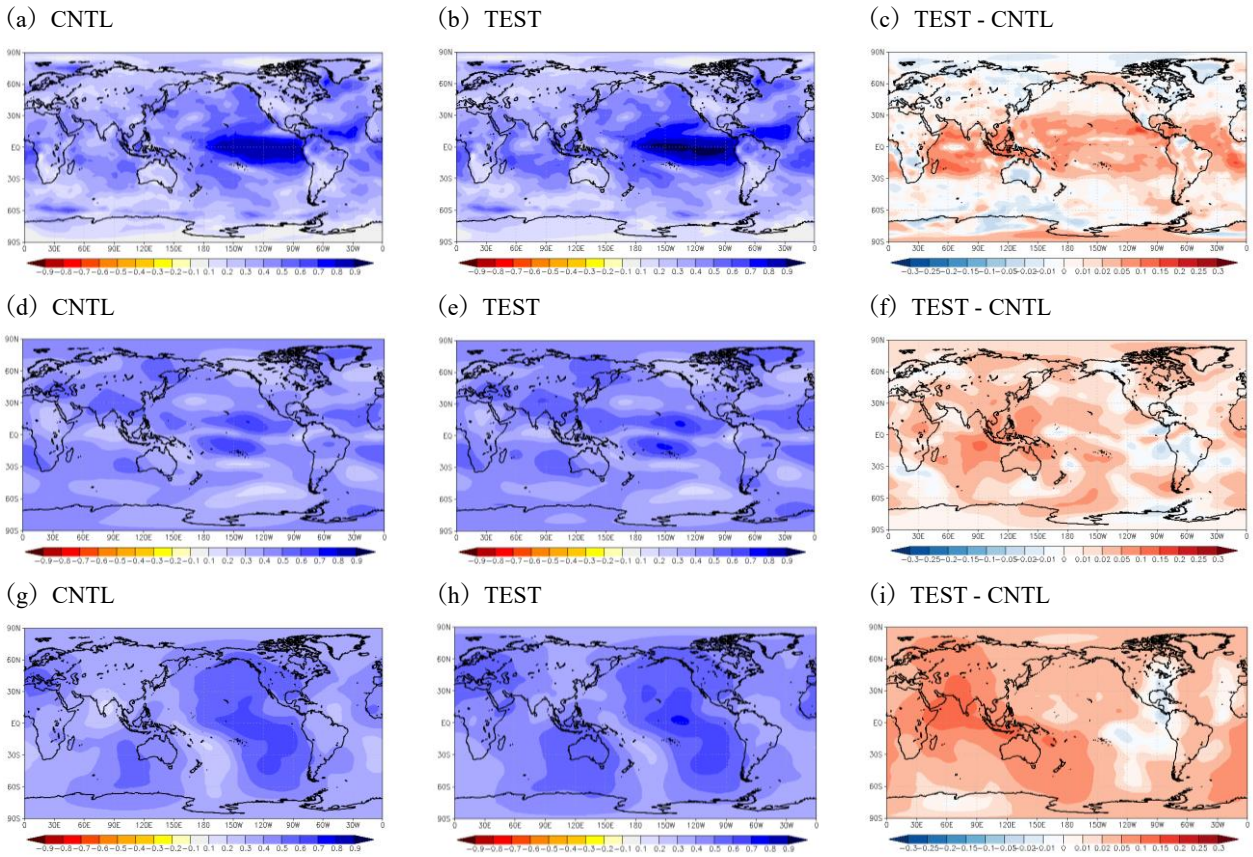


**Fig. 1** Ensemble-mean anomaly correlation coefficient averaged for all initial dates over weeks 3 and 4 for (a) – (c) surface temperature, (d) – (f) 200-hPa stream function, and (g) – (i) 200-hPa velocity potential. Left: CNTL experiment; center: TEST experiment; right: difference between TEST and CNTL.

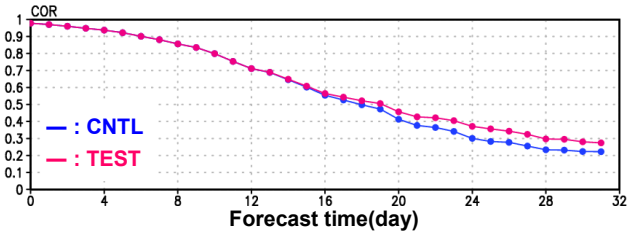


**Fig. 2** Correlation of MJO index (Matsueda and Endo, 2011) for the case that the amplitude is above 1 at an initial date in winter (from November to April). Red line; TEST experiment; blue line: CNTL experiment.

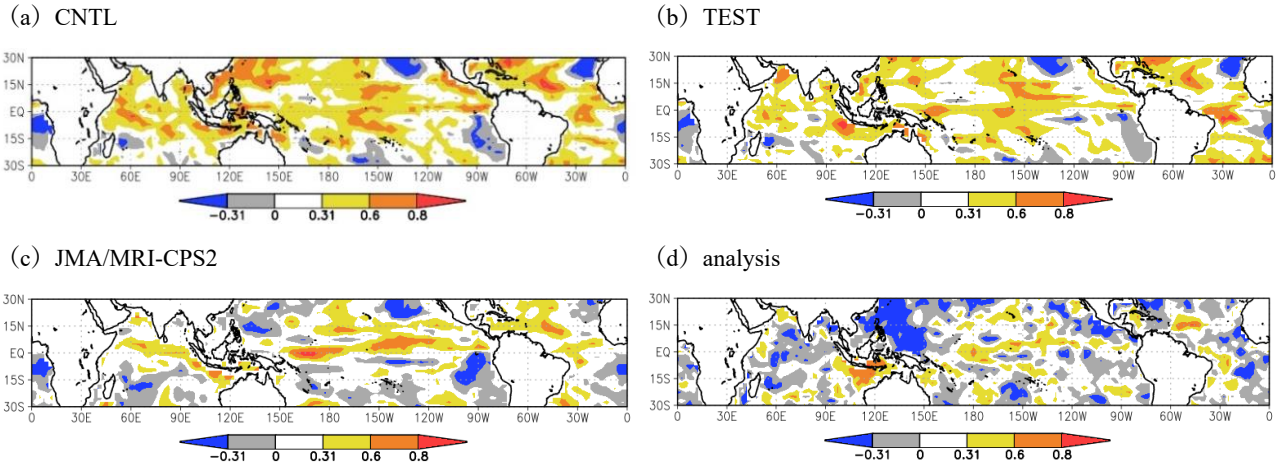


**Fig.3** Correlation of SST and precipitation over week 4 on 30th June. The correlation of (d) is calculated under the Global Precipitation Climatology Project (GPCP: Huffman et al., 2001) and MGDSST (Kurihara et al., 2006)

# Upgrade of JMA's Global Ensemble Prediction System

YAMAGUCHI Haruki, IKEGAMI Masaaki, OCHI Kenta, OTA Yoichiro, SEKIGUCHI Ryohei, and TAKAKURA Toshinari

Japan Meteorological Agency
e-mail: h.yamaguchi@met.kishou.go.jp

## 1. Introduction

The Japan Meteorological Agency (JMA) upgraded its Global Ensemble Prediction System (Global EPS) on March 24 2020 to incorporate recent developments in the Global Spectral Model (GSM), a two-tiered sea surface temperature (SST) approach and a direct application of initial perturbations from JMA's new hybrid data assimilation system.

## 2. Major updates

### (1) Incorporation of recent GSM developments

The forecast model for the Global EPS was upgraded to a low-resolution version of the newly revised Global Spectral Model (GSM; Yonehara et al. 2020). Sharing the same version of the forecast model with GSM enabled updating with the latest developments made since the introduction of the Global EPS in 2017.

### (2) Two-tiered SST approach

SST as a lower-boundary condition for the forecast model with a lead time of 12 days was improved by adopting a two-tiered SST approach (Takakura and Komori 2020), while the SST within lead times of 11 days was prescribed as a persisting anomaly from the climatological SST as per the previous Global EPS.

### (3) Changes in initial perturbations

The initial perturbations from the Local Ensemble Transform Kalman Filter (LETKF) are directly produced from JMA's new hybrid data assimilation (Kadowaki et al., 2020), instead of the independent LETKF cycle of the previous Global EPS. The amplitude of singular vector (SV)-based initial perturbations targeted in the high- and mid-latitudes of both hemispheres was reduced by 8.7% to mitigate over-dispersiveness in 500 hPa geopotential height forecasts with lead times of up to four days. SVs calculated over desert areas in low latitudes, resulting in irrational humidity perturbations over climatologically dry areas, are removed when such SVs are composed to form initial perturbations.

## 3. Verification results

To verify the performance of the new system for medium-range forecasting with lead times of up to 11 days, retrospective experiments covering periods exceeding three months in summer 2018 and winter 2017/18 were conducted. The results showed improvements in the RMSEs of ensemble mean forecasts for several elements, including 850 hPa temperature, 500 hPa geopotential height and 200 hPa winds, for both seasons. Figure 1 shows values for 500 hPa geopotential height in winter. Winter Brier skill scores for precipitation forecasts in Japan were also improved (not shown).

The hindcast experiments were also conducted for the 30-year period from 1981 to 2010 with data

from the Japanese 55-year Reanalysis (JRA-55; Kobayashi et al. 2015) as atmospheric initial conditions. Mean forecast errors were reduced over the Tropics (20°S – 20°N) in particular. For anomaly correlation coefficients of velocity potential at 200 hPa over the Tropics, the new Global EPS demonstrates improved forecast skill for most lead times and seasons (Figure 2). MJO forecast skill in areas such as correlation was also improved on sub-seasonal to seasonal timescales, benefiting from the two-tiered SST approach (not shown).

References


Kadowaki, T., Y. Ota, and S. Yokota, 2020: Introduction of a new hybrid data assimilation system for the JMA Global Spectrum Model. *CAS/JSC WGNE Res. Activ. Atmos. Oceanic Modell.*, submitted.

Kobayashi, S., Y. Ota, Y. Harada, A. Ebita, M. Moriya, H. Onoda, K. Onogi, H. Kamahori, C. Kobayashi, H. Endo, K. Miyaoka, and K. Takahashi, 2015: The JRA-55 reanalysis: General specifications and basic characteristics. J. Meteor. Soc. Japan., 93, 5-48.

Yonehara, H., and C. Matsukawa, T. Nabetani, T. Kanehama, T. Tokuhiro, K. Yamada, R. Nagasawa, Y. Adachi, and R. Sekiguchi, 2020: Upgrade of JMA's Operational Global Model. *CAS/JSC WGNE Res. Activ. Atmos. Oceanic Modell.*, submitted.

Takakura, T., and T. Komori, 2020: Two-tiered sea surface temperature approach implemented to JMA's Global Ensemble Prediction System. *CAS/JSC WGNE Res. Activ. Atmos. Oceanic Modell.*, submitted.


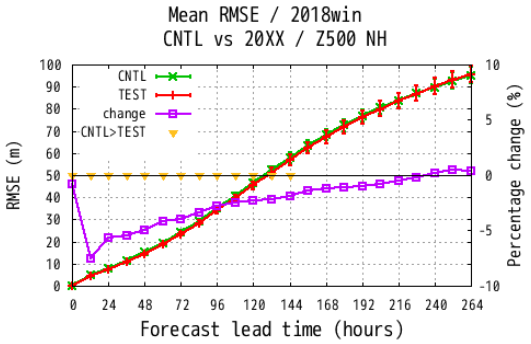


Figure 1: RMSEs of ensemble mean forecasts for 500 hPa geopotential height in the Northern Hemisphere (20°N – 90°N) during winter 2017/18 as a function of forecast lead times up to 264 hours. The red and green lines represent verification results for the new (TEST) and previous (CNTL) Global EPS (left axis; unit: m), and the purple line represents rates of change in scores ([TEST – CNTL]/CNTL, right axis; unit: %). Error bars indicate two-sided 95% confidence levels, and triangles indicate a statistically significant difference of 0.05.

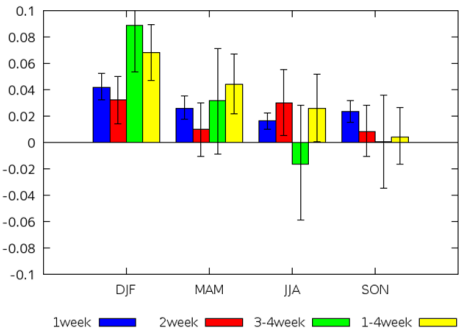


Figure 2: Differences in anomaly correlation coefficients for velocity potential at 200 hPa in the Tropics (20°S – 20°N) for all seasons. Positive values represent Global EPS anomaly correlation coefficients exceeding those of the previous Global EPS. Error bars indicate two-sided 95% confidence levels.

# Upgrade of JMA's Operational Global Model

YONEHARA Hitoshi, MATSUKAWA Chihiro, NABETANI Takashi, KANEHAMA Takafumi, TOKUHIRO Takayuki, YAMADA Kazutaka, NAGASAWA Ryoji, ADACHI Yukimasa, and SEKIGUCHI Ryouhei

Japan Meteorological Agency, Tokyo, Japan

(email: yonehara@met.kishou.go.jp)

## 1. Introduction

In March 2020, the Japan Meteorological Agency (JMA) upgraded its operational Global Spectral Model (GSM; JMA 2019). The revision involved the refinement of parametrized surface drag processes, land surface processes, and surface albedo and stratocumulus on sea ice, which collectively resulted in better forecasting than with previous versions (Yonehara et al. 2018), especially in Northern Hemisphere middle and high latitudes. This report outlines individual components of the upgrade and related verification results.

## 2. Major updates

### 2.1 Parametrized surface drag processes

The subgrid-scale orography (SSO) scheme proposed by Lott and Miller (1997) replaced the previous scheme proposed by Iwasaki et al. (1989). The new version represents low-level blocked-flow drag produced by lateral flow that goes around subgrid-scale orography. The flow over such orography generates gravity waves, which vertically transport and deposit momentum where waves break. On top of this, the turbulent orographic form drag (TOFD) scheme (Beljaars et al. 2004) was also introduced. The introduction of the new set of schemes reduced forecast errors around troughs and ridges in the lower and middle troposphere over Northern Eurasia.

### 2.2 Land surface processes

The upgrade of land surface processes includes changes in the fraction of snow coverage (Roesch et al. 2001) and diagnostic schemes for soil thermal conductivity (Ek et al. 2003) to address various surface biases. The former appropriately reduced the diagnosed fraction of snow coverage, and the latter resulted in a relative suppression of excessive diurnal amplitude of soil heat flux. These updates resulted in a reduction of the excessive sensible heat flux seen in the previous land surface processes.

### 2.3 Surface albedo and stratocumulus on sea ice

To correct lower surface albedo biases in the Arctic, a new sea ice albedo scheme incorporating the effects of snow (Hunke and Lipscomb 2006) was introduced with a climatological snow cover fraction.

The diagnostic stratocumulus generation scheme (Kawai and Inoue 2006) was also disabled for sea ice areas to correct for excess cloud cover.

## 3. Verification results

Twin experiments were conducted to compare forecast scores of the previous (CNTL) and updated models (TEST) for July to September 2018 and December to February 2017/2018. Figure 1 shows root-mean-square error (RMSE) differences for 500-hPa geopotential height forecasts up to 5.5 days ahead verified against radiosonde observations averaged over the Northern Hemisphere (20 – 90°N) for both periods. Figure 2 shows mean errors (MEs) of 500-

hPa geopotential height at T+3d for CNTL and TEST. The upgraded system improved RMSE and ME values over forecasts of several days than previous GSM versions.

**References**


Beljaars, A., A. R. Brown, and N. Wood., 2004: A new parametrization of turbulent orographic form drag. Q. J. R. Meteorol. Soc., 130, 1327-1347.

Ek, M. B., K. E. Mitchell, Y. Lin, E. Rogers, P. Grunmann, V. Koren, G. Gayno, and J. D. Tarpley, 2003: Implementation of Noah land surface model advances in the National Centers for Environmental Prediction operational mesoscale Eta model. J. Geophys. Res., 108, 8851.

Hunke, E. C., and W. H. Lipscomb, 2006: CICE: the Los Alamos Sea Ice Model Documentation and Software User's Manual. http://oceans11.lanl.gov/trac/CICE.

Iwasaki, T., S. Yamada, and K. Tada, 1989: A Parameterization Scheme of Orographic Gravity Wave Drag with Two Different Vertical Partitionings Part I: Impacts on Medium-Range Forecasts. J. Meteor. Soc. Japan, 67, 11-27.

Japan Meteorological Agency, 2019: Outline of Operational Numerical Weather Prediction at JMA. Japan Meteorological Agency, Tokyo, Japan.

Kawai, H., and T. Inoue, 2006: A simple parameterization scheme for subtropical marine stratocumulus. SOLA, 2, 17–20.

Lott, F. and M. J. Miller, 1997: A new subgrid‐scale orographic drag parametrization: Its formulation and testing. Q. J. R. Meteorol. Soc., 123, 101-127.

Roesch, A., M. Wild, H. Gilgen, and A. Ohmura, 2001: A snow cover fraction parametrization for the ECHAM4 GCM. Climate Dyn., 17, 933–946.

Yonehara H., R. Sekiguchi, T. Kanehama, K. Saitou, T. Kinami, A. Shimokobe, D. Hotta, R. Nagasawa, H. Sato, M. Ujiie, T. Kadowaki, S. Yabu, K. Yamada, M. Nakagawa, T. Tokuhiro, 2018, Upgrade of JMA's operational global NWP system, CAS/JSC WGNE Res. Activ. Atmos. Oceanic Modell., 4.17 – 4.18.


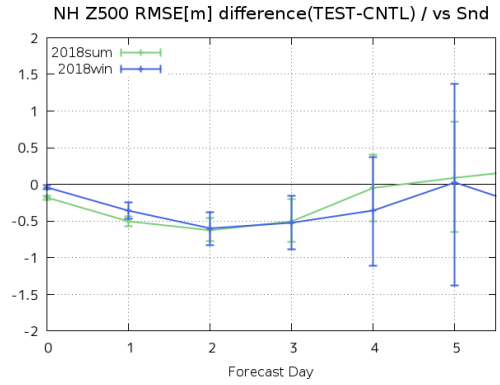


Figure 1. Root-mean-square error differences (TEST – CNTL) of 500-hPa geopotential height [m] against radiosonde (Snd) in the Northern Hemisphere extra-tropics (20 – 90°N) in the summer and winter experiments. The horizontal axis shows the forecast lead time [days], and the green and blue lines show the summer and winter experiments, respectively. Error bars indicate statistical significance with 95% confidence based on the bootstrap method.

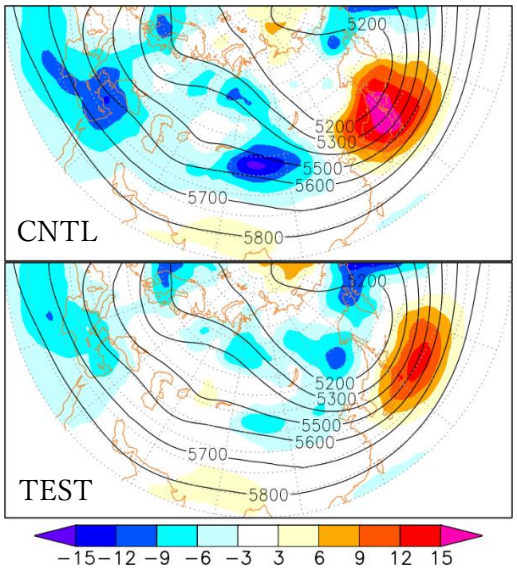


Figure 2. Mean errors of 500-hPa geopotential height [m] at T+3d in the 0 – 180°E, 20 – 90°N region for the winter experiment (shading). Contours represent time-averaged analysis.